

# Isotropic color gradient for simulating very high-density ratios with a two-phase flow lattice Boltzmann model

Sébastien Leclaire\*, Marcelo Reggio, Jean-Yves Trépanier

Department of Mechanical Engineering, École Polytechnique, 2500, Chemin de Polytechnique, Montreal, Quebec, Canada H3T 1J4

## ARTICLE INFO

### Article history:

Received 2 October 2010

Received in revised form 10 March 2011

Accepted 3 April 2011

Available online 27 April 2011

### Keywords:

Lattice Boltzmann method  
Immiscible two-phase flow  
Isotropic gradient  
Color gradient  
Surface tension  
High-density ratio  
Spurious current  
Laplace's law

## ABSTRACT

This study presents the integration of isotropic color gradient discretization into a lattice Boltzmann Rothman–Keller (RK) model designed for two-phase flow simulation. The proposed model removes one limitation of the RK model, which concerns the handling of  $O(1000)$  large density ratios between the fluids for a wide range of parameters. Taylor's series expansions are used to characterize the difference between an isotropic gradient discretization and the commonly used anisotropic gradient. The proposed color gradient discretization can reduce, by one order of magnitude, the spurious current problem that affects the interface between the phases. A set of numerical tests is conducted to show that a rotationally invariant discretization enables widening of the parameter range for the surface tension. Surface tensions from  $O(10^{-2})$  to  $O(10^{-8})$ , depending on the density ratio, are accurately simulated. An extreme density ratio of  $O(10,000)$  is successfully tested for a steady bubble with an error of 0.5% for Laplace's law across a sharp interface, with a thickness of about 5–6 lattice units.

© 2011 Elsevier Ltd. All rights reserved.

## 1. Introduction

For two decades now, a new method for examining fluids in the molecular state, rather than at the classical macroscopic level, has been developed and used as a tool for numerical flow simulation. This alternative, known as the lattice Boltzmann method (LBM), uses continuous distribution functions [1], and was originally built as an extension of the lattice gas automata [2]. Later, it was discovered that the method can also be regarded as a systematic truncation of the Boltzmann equation in the velocity space [3]. The advantages of the LBM are the way in which it addresses computational issues in complex geometries, and that it is simple to apply, because the streaming operator is linear.

One of the features of the LBM is its great flexibility in dealing with additional complex physics, which is difficult for the traditional CFD methods, based on the Navier–Stokes equations, to handle. Multiphase flow is a typical example of such complex physics. In this case, even some existing LBMs still face problems because of their limited parameter window with respect to surface tension and density ratio, which hampers its application in practical engineering problems. Before setting out the specific goal of this study, we briefly recall the techniques commonly used to predict multiphase flows within the lattice Boltzmann framework.

The lattice Boltzmann (LB) models for immiscible two-phase flows can generally be classified in five groups: Rothman–Keller (RK) [4–13], Shan–Chen (SC) [14], Free Energy (FE) [15,16], mean-field (MF) [17,18], and field mediator (FM) [19].

The original RK model considers two types of fluids, red and blue, each of them with particle distributions following its own LB equation. Because there are two fluids involved, the collision step, intrinsic to any LB formulation, takes into account interactions among particles of the same color, as well as cross interactions between particles of different colors. These latter are related to the surface tension between the two phases, which requires the gradient of the color function. The phase separation is achieved with an additional recoloring step. For the original RK models, this step is seen as cumbersome to program. Recently, however, the ideas of Latva-Kokko and Rothman [7] have made it very easy and straightforward to implement, along with the additional capability of interface thickness adjustment. Work to introduce thermodynamics into the RK model has also been carried out, by Kono et al. [20].

The model developed by Shan and Chen [14] uses an interaction force between the particles to mimic microscopic interactions and automatically separate the concentrated and diluted phases. This spontaneous phase segregation is a feature that has attracted LB practitioners and contributed to the popularity of the SC model.

The free energy method of Swift et al. [15] describes an approach which, in equilibrium, leads to a steady state that can be associated with a free energy. The method uses collision rules,

\* Corresponding author.

E-mail address: [sebastien.leclaire@polymtl.ca](mailto:sebastien.leclaire@polymtl.ca) (S. Leclaire).

which ensure that the system evolves towards the minimum of an input free energy functional. This functional includes both the pure fluid part and the interface part. The first accounts for the equilibrium between two phases, while the second concerns surface tension. Like the SC model, this formulation is also capable of achieving automatic phase separation.

The MF methods simulate interparticle attraction in the same way as the Coulomb interaction is treated in the Vlasov equation [17]. These models can simulate thermodynamically consistent liquid–vapor systems, where the SC models fail [21].

The FM methods use null-mass particles, the only role of which is to invert the momentum of lattice particles in the transition layer to segregate fluids of different colors [19]. They have the advantage of being able to incorporate binary diffusivity, and this method can therefore be adapted to simulate miscible fluids.

A major problem common to these five methods is that they all appear to suffer from the presence of spurious currents at the interface between the fluids. These currents affect numerical stability, limit the density ratio, and reduce accuracy.

Spurious currents at a two-fluid interface in the RK method have been studied by Ginzbourg and Adler [6], who noted that an appropriate choice of the eigenvalues of the collision matrix leads to the elimination of these currents under certain circumstances. Unfortunately, the authors conclude that these unrealistic currents cannot be eliminated or reduced solely with the choice of eigenvalues. The spurious current phenomenon near an interface has also been mentioned by Halliday et al. in [5], where it was found that these currents are strongest at the interface between two fluids. To reduce them, Dupin et al. [10] proposed adjusting the surface tension between the fluids by disturbing the distribution functions in accordance with the directions of the lattice. This idea seemed promising, but has not been further explored.

In this paper, an improvement to the RK-type model, described in Refs. [4,22], is proposed which reduces spurious currents. It should be noted that the methodology presented here can be applied to any RK-type LB model.

A characteristic that distinguishes the RK model from other models is the presence of a color gradient. For two-phase LB flows, the color gradient was introduced by Rothman and Keller [23] with their model based on cellular automata. It is by using the color gradient that the interface between the fluids is maintained, and evaluating the color gradient is the key point that we address in this study. Specifically, the goal of this work is to show that an isotropic discretization of the color gradient, that is, with a leading discretization error that is rotationally invariant [24], increases the robustness of the method. This is of primary importance, because it ensures less accumulation of directionally biased discretization errors, and one consequence of using it is a reduction in spurious currents. This ultimately means that it will be possible to solve problems with a higher density ratio and/or with lower surface tension than previously achieved with other RK-type models.

Another challenge facing LBMs designed to simulate two-phase flows is handling the high-density ratio between the phases. Ratios of  $O(160)$  were simulated by Kuzmin and Mohamad [25] using a multi-range, multi-relaxation time LB scheme. However, this improved SC method is still unable to simulate a  $O(1000)$  air-to-water density ratio. With the projection method, an FE scheme devised by Inamuro et al. [26,27] succeeded in simulating density ratios of up to  $O(1000)$ . Unfortunately, this method requires the solution of a costly Poisson equation at every time step. Other methods, such as the one proposed by Lee and Lin [28], can treat high-density ratios, like  $O(1000)$ , using a special discretization of the LB equation. Although it seems quite complex, this discretization works well, according to the authors. Another promising approach has been developed by Zheng et al. [29], which can also achieve  $O(1000)$  density ratios and does not require the solution of a Pois-

son equation or the implementation of a complex treatment of derivatives. More recently, Becker et al. [30] succeeded in simulating density ratios as high as  $O(1000)$  using the LBM and the level set method. However, coupling the LBM and the level set method is not straightforward, because doing so requires knowledge from two different research fields.

The RK model has been shown to be capable of simulating complex two-phase flow problems, but with density ratios reaching only  $O(80)$  [4]. Our study will show that this limit can be substantially increased. The method is based on a modified recoloring operator presented by Leclaire et al. [4], which, when combined with the improvement presented in this work, can handle high-density ratios, up to  $O(10,000)$ , with great accuracy for Laplace's law. Specifically, the model is based on that of Reis and Phillips [22], with a variant of the recoloring operator from Latva-Kokko and Rothman [7]. This improvement is expected to allow high-density ratios to be addressed for all RK models.

When applying the RK method, anisotropic color gradients are mostly used [5,11,10,9,7,6,31,13]. In fact, an isotropic color gradient is seldom used, and can only be found in [12,32]. Unfortunately, in these studies, neither the advantage of using such a gradient discretization, nor the reason for doing so, is explained.

In contrast, for the three LBMs for multiphase flows, FE, MF, and SC, isotropic gradients have been used. For the FE methods, Tiribocchi et al. [33] show that there is a reduction in the spurious current by one order of magnitude when the gradient in the source term of their model is defined using a rotationally invariant discretization. Spurious currents were also reduced in the work of Pooley and Furtado [34] when an isotropic gradient is used, along with the addition of a special forcing term.

More recently, Chiappini et al. [35] proposed an MF model which completely eliminates spurious currents, but, unfortunately, the model does not respect the principle of mass conservation.

Similarly, isotropic discretizations have been introduced for the SC methods [36] for the gradient of the “effective mass function”, represented by the interparticle interactions. Again, it is shown that the more isotropy there is in the gradient, the lower the spurious currents. A detailed description of isotropic gradient stencils and weights can be found in the work of Sbragaglia et al. [37] for 2D and 3D spaces.

In this paper, we present the development of a second order color gradient discretization, while for higher order gradients, the stencils and weights developed by Sbragaglia et al. [37] will be used. This choice will make it possible to improve the accuracy of the RK model presented in [4]. To our knowledge, there is no study showing that the implementation of an isotropic color gradient in RK models provides a significant reduction in spurious currents, widens the range of application of the surface tension, or greatly increases the maximum density ratio handled between the two phases.

This paper is organized in two major sections. In the first, the LB model is given, along with theoretical details to illustrate the difference between isotropic and anisotropic gradients. In the second, a large number (hundreds) of numerical simulations are performed for a steady bubble, combining the various parameters of the model. These tests allow us to analyze the influence of gradient discretization on the solution and to demonstrate the need for an isotropic gradient, and its superiority, versus the standard anisotropic approximation. The primary goal of our paper is to demonstrate the usefulness of an isotropic gradient discretization for the RK model.

## 2. Lattice Boltzmann immiscible two-phase model

The current LB approach follows the model of Reis and Phillips [22], along with the improvement presented by Leclaire et al. [4]

for the recoloring operator. For the sake of clarity, we recall the model described in Refs. [4,22]. For this two-dimensional LB model, there are two sets of distribution functions, one for each fluid, moving on a D2Q9 grid with the velocity vectors  $\vec{c}_i$ . With  $\theta_i = \frac{\pi}{4}(4-i)$ , the velocity vectors are defined as ( $\Delta x = \Delta y = 1$ ):

$$\vec{c}_i = \begin{cases} (0, 0), & i = 1 \\ [\sin(\theta_i), \cos(\theta_i)], & i = 2, 4, 6, 8 \\ [\sin(\theta_i), \cos(\theta_i)]\sqrt{2}, & i = 3, 5, 7, 9 \end{cases} \quad (1)$$

The distribution functions for a fluid of color  $k$  (with  $k = r$  for red or  $k = b$  for blue) are noted  $N_i^k(\vec{x}, t)$ , while  $N_i(\vec{x}, t)$  is used for the sum  $N_i^r(\vec{x}, t) + N_i^b(\vec{x}, t)$ . If the time step is  $\Delta t = 1$ , the algorithm uses the following evolution equation:

$$N_i^k(\vec{x} + \vec{c}_i, t + 1) = N_i^k(\vec{x}, t) + \Omega_i^k(N_i^k(\vec{x}, t)) \quad (2)$$

where the collision operator  $\Omega_i^k$  is the result of the combination of three sub operators (similar to Ref. [11]):

$$\Omega_i^k = (\Omega_i^k)^{(3)} \left[ (\Omega_i^k)^{(1)} + (\Omega_i^k)^{(2)} \right] \quad (3)$$

In the algorithm, the evolution equation is solved in four steps with operator splitting, as follows:

1. Single-phase collision operator:

$$N_i^k(\vec{x}, t_*) = (\Omega_i^k)^{(1)}(N_i^k(\vec{x}, t))$$

2. Two-phase collision operator (perturbation):

$$N_i^k(\vec{x}, t_{**}) = (\Omega_i^k)^{(2)}(N_i^k(\vec{x}, t_*))$$

3. Two-phase collision operator (recoloring):

$$N_i^k(\vec{x}, t_{***}) = (\Omega_i^k)^{(3)}(N_i^k(\vec{x}, t_{**}))$$

4. Streaming operator:

$$N_i^k(\vec{x} + \vec{c}_i, t + 1) = N_i^k(\vec{x}, t_{***})$$

### 2.1. Single-phase collision operator

The first sub operator,  $(\Omega_i^k)^{(1)}$ , is the standard BGK operator of the single-phase LBM, where the distribution functions are relaxed towards a local equilibrium in which  $\omega_k$  denotes the relaxation factor:

$$(\Omega_i^k)^{(1)}(N_i^k) = N_i^k - \omega_k(N_i^k - N_i^{k(e)}) \quad (4)$$

Here, some details concerning this operator are given. The density of the fluid  $k$  is given by the first moment of the distribution functions:

$$\rho_k = \sum_i N_i^k = \sum_i N_i^{k(e)} \quad (5)$$

where the superscript  $(e)$  denotes equilibrium. The total fluid density is given by  $\rho = \rho_r + \rho_b$ , while the total momentum is defined as the second moment of the distribution functions:

$$\rho \vec{u} = \sum_i \sum_k N_i^k \vec{c}_i = \sum_i \sum_k N_i^{k(e)} \vec{c}_i \quad (6)$$

in which  $\vec{u}$  is the density weighted average velocity of the fluid. The equilibrium functions are defined by [22]:

$$N_i^{k(e)} = \rho_k \left( \phi_i^k + W_i \left[ 3\vec{c}_i \cdot \vec{u} + \frac{9}{2}(\vec{c}_i \cdot \vec{u})^2 - \frac{3}{2}(\vec{u})^2 \right] \right) \quad (7)$$

These equilibrium distribution functions  $N_i^{k(e)}$  are chosen to respect the principles of mass and momentum conservation. The weights  $W_i$  are those of a standard D2Q9 lattice:

$$W_i = \begin{cases} 4/9, & i = 1 \\ 1/9, & i = 2, 4, 6, 8 \\ 1/36, & i = 3, 5, 7, 9 \end{cases} \quad (8)$$

Besides,

$$\phi_i^k = \begin{cases} \alpha_k, & i = 1 \\ (1 - \alpha_k)/5, & i = 2, 4, 6, 8 \\ (1 - \alpha_k)/20, & i = 3, 5, 7, 9 \end{cases} \quad (9)$$

As introduced in [9], in order to obtain a stable interface, the density ratio  $\gamma$  is defined by:

$$\gamma = \frac{\rho_r}{\rho_b} = \frac{1 - \alpha_b}{1 - \alpha_r} \quad (10)$$

Without loss of generality,  $\rho_r \geq \rho_b$  in this paper. The pressure of the fluid of color  $k$  is:

$$p^k = \frac{3\rho_k(1 - \alpha_k)}{5} = \rho_k(c_s^k)^2 \quad (11)$$

where, in the above expressions, either  $\alpha_r$  or  $\alpha_b$  represents a free parameter, and  $c_s^k$  is the sound speed in the fluid of color  $k$  [22,38].

The relaxation parameters  $\omega_k$  are chosen so that the evolution Eq. (2) respects the macroscopic equations for single-phase flow in the single-phase regions [22]. This parameter is a function of the fluid viscosity  $\nu_k$ , given by  $\omega_k = 1/(3\nu_k + \frac{1}{2})$ . As introduced in [9], when the viscosities of the fluids are different, an interpolation is applied to define the parameter  $\omega_k$  at the interface. To do this, it is necessary to introduce the color field:

$$\psi = \frac{\rho_r - \rho_b}{\rho_r + \rho_b} \quad (12)$$

The color field  $\psi$  is a function with its image between  $-1$  and  $1$ . It takes the value  $1$  or  $-1$ , depending on whether it is evaluated at a position that contains only the red fluid or only the blue fluid. At an interface, the color field is obviously between  $-1$  and  $1$ . The relaxation factor  $\omega_k$  in Eq. (4) is replaced by  $\omega$ :

$$\omega = \begin{cases} \omega_r, & \psi > \delta \\ f_r(\psi), & \delta \geq \psi > 0 \\ f_b(\psi), & 0 \geq \psi \geq -\delta \\ \omega_b, & \psi < -\delta \end{cases} \quad (13)$$

in which  $\delta$  is a free parameter and

$$\begin{aligned} f_r(\psi) &= \chi + \eta\psi + \kappa\psi^2 \\ f_b(\psi) &= \chi + \lambda\psi + \nu\psi^2 \end{aligned} \quad (14)$$

with

$$\begin{aligned} \chi &= 2\omega_r\omega_b/(\omega_r + \omega_b) \\ \eta &= 2(\omega_r - \chi)/\delta \\ \kappa &= -\eta/(2\delta) \\ \lambda &= 2(\chi - \omega_b)/\delta \\ \nu &= \lambda/(2\delta) \end{aligned} \quad (15)$$

The free parameter  $\delta$  is required to calculate  $\omega$ , and influences the thickness of the interface when the fluid viscosities are different [22]. The larger  $\delta$ , the thicker the fluid interface. If the fluid viscosities are the same, the parameter  $\delta$  does not have an impact on the solution, because, in this case,  $\omega = \omega_r = \omega_b$ .

## 2.2. Perturbation operator

In the RK model, surface tension is modeled by means of the perturbation operator [5,22,39]. In this model, with  $F$ , the color gradient in terms of the color difference, the perturbation operator, is defined by:

$$(\Omega_i^k)^{(2)}(N_i^k) = N_i^k + \frac{A_k}{2} |\vec{F}| \left[ W_i \frac{(\vec{F} \cdot \vec{c}_i)^2}{|\vec{F}|^2} - B_i \right] \quad (16)$$

where

$$B_i = \begin{cases} -4/27, & i = 1 \\ 2/27, & i = 2, 4, 6, 8 \\ 5/108, & i = 3, 5, 7, 9 \end{cases} \quad (17)$$

Reis and Phillips [22] have shown that this operator complies with the macroscopic equations for two-phase flows. It handles the coupling between the two fluids, with the free parameters  $A_k$  chosen to model the surface tension. Although this operator generates the surface tension, it does not guarantee the fluid's immiscibility. To minimize the mixing and segregate the two fluids, the recoloring operator  $(\Omega_i^k)^{(3)}$  needs to be properly selected. This process is introduced in the next subsection. But first, some insight concerning the discretization of the color gradient is needed.

### 2.2.1. Standard anisotropic color gradient

The color gradient direction is an approximation of the perpendicular to the interface between the fluids. Usually, the color gradient in the RK model is defined by:

$$\vec{F}(\vec{x}) = \sum_i \vec{c}_i (\rho_r(\vec{x} + \vec{c}_i) - \rho_b(\vec{x} + \vec{c}_i)) = \sum_i \vec{c}_i \Delta(\vec{x} + \vec{c}_i) \quad (18)$$

with  $\Delta = \rho_r - \rho_b$  introduced to simplify the following derivation. Without loss of generality, the function  $\Delta$  is expressed using a two-dimensional Taylor series expansion around the zero vector:

$$\begin{aligned} \Delta(x, y) = \Delta(0, 0) &+ x \frac{\partial \Delta}{\partial x} \Big|_{(0,0)} + y \frac{\partial \Delta}{\partial y} \Big|_{(0,0)} + \frac{1}{2} x^2 \frac{\partial^2 \Delta}{\partial x^2} \Big|_{(0,0)} + xy \frac{\partial^2 \Delta}{\partial x \partial y} \Big|_{(0,0)} \\ &+ \frac{1}{2} y^2 \frac{\partial^2 \Delta}{\partial y^2} \Big|_{(0,0)} + \frac{1}{6} x^3 \frac{\partial^3 \Delta}{\partial x^3} \Big|_{(0,0)} + \frac{1}{2} x^2 y \frac{\partial^3 \Delta}{\partial x^2 \partial y} \Big|_{(0,0)} \\ &+ \frac{1}{2} xy^2 \frac{\partial^3 \Delta}{\partial x \partial y^2} \Big|_{(0,0)} + \frac{1}{6} y^3 \frac{\partial^3 \Delta}{\partial y^3} \Big|_{(0,0)} + O(x^n y^m) \end{aligned}$$

with  $n + m > 3$ . To approximate the gradient in the  $x$  direction, the following stencil values, marked with a “red cross” in Fig. 1, can be taken:  $\Delta(h, h)$ ,  $\Delta(h, 0)$ ,  $\Delta(h, -h)$ ,  $\Delta(-h, -h)$ ,  $\Delta(-h, 0)$ , and  $\Delta(-h, h)$ .

When these stencil values are combined, as in the case of the standard anisotropic color gradient (Eq. (18)), an approximation of the gradient in the  $x$  direction at  $(0, 0)$  is obtained:

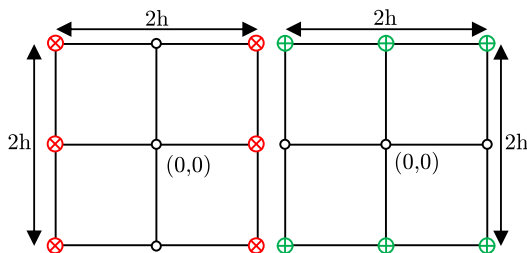


Fig. 1. Stencil points.

$$\begin{aligned} \frac{\partial \Delta}{\partial x} \Big|_{(0,0)} &= \frac{1}{6h} [\Delta(h, h) + \Delta(h, 0) + \Delta(h, -h) - \Delta(-h, -h) - \Delta(-h, 0) \\ &\quad - \Delta(-h, h)] - \frac{h^2}{6} \frac{\partial^3 \Delta}{\partial x^3} \Big|_{(0,0)} - \frac{h^2}{3} \frac{\partial^3 \Delta}{\partial x^2 \partial y} \Big|_{(0,0)} + O(h^3) \end{aligned} \quad (19)$$

Using the stencil values marked with a “green plus sign” in Fig. 1, a similar expression is found for the  $y$  direction:

$$\begin{aligned} \frac{\partial \Delta}{\partial y} \Big|_{(0,0)} &= \frac{1}{6h} [\Delta(-h, h) + \Delta(0, h) + \Delta(h, h) - \Delta(h, -h) - \Delta(0, -h) \\ &\quad - \Delta(-h, -h)] - \frac{h^2}{6} \frac{\partial^3 \Delta}{\partial y^3} \Big|_{(0,0)} - \frac{h^2}{3} \frac{\partial^3 \Delta}{\partial x \partial y^2} \Big|_{(0,0)} + O(h^3) \end{aligned} \quad (20)$$

In the approximate gradients of Eqs. (19) and (20), the leading differential operator of the second order error term ( $O(h^2)$ ) can be written in vector form:

$$\vec{E}^{(2)} = -\frac{h^2}{6} \left[ \frac{\partial^3}{\partial x^3} + 2 \frac{\partial^3}{\partial x^2 \partial y} \cdot \frac{\partial^3}{\partial y^3} + 2 \frac{\partial^3}{\partial x \partial y^2} \right] \quad (21)$$

Using the following partial derivative operator transformation:

$$\frac{\partial}{\partial x} = \cos(\theta) \frac{\partial}{\partial r} - \frac{1}{r} \sin(\theta) \frac{\partial}{\partial \theta} \quad (22)$$

$$\frac{\partial}{\partial y} = \sin(\theta) \frac{\partial}{\partial r} + \frac{1}{r} \cos(\theta) \frac{\partial}{\partial \theta} \quad (23)$$

and by supposing that  $\Delta = \Delta(r)$ , it is possible to show (after a lengthy algebraic manipulation) that, when the differential operator  $\vec{E}^{(2)}$  is applied to  $\Delta(r)$ , the resulting vector will have a Euclidean norm that is a function of  $\theta$  and  $r$ , except if  $\Delta(r)$  is a constant. This result, that is, the norm  $\|\vec{E}^{(2)} \Delta(r)\| \equiv f(r, \theta)$ , is an equation that takes up almost a page and so is not presented here. This result can easily be obtained with symbolic mathematics software. For a vector function to be rotationally invariant, it must have a Euclidean norm that is a function of the radius only. Therefore, this color gradient approximation is not isotropic to the second order in space, but anisotropic. It is worth noting that, even if the function  $\Delta$  is isotropic (i.e.  $\Delta = \Delta(r)$ ) around  $(0, 0)$ , the calculated derivatives have an error leading term that is not isotropic. This means that, when the color gradient is approximated with this finite difference stencil, the color gradient calculated will not conserve the isotropic property of the differentiated function.

### 2.2.2. Isotropic color gradient

Taking into consideration the anisotropy problem of the standard color gradient, it is possible to change the weights of the grid points when computing the gradient to make them isotropic up to the second order in space by defining the gradients in the  $x$  and  $y$  directions, as follows:

$$\begin{aligned} \frac{\partial \Delta}{\partial x} \Big|_{(0,0)} &= \frac{1}{12h} [\Delta(h, h) + 4\Delta(h, 0) + \Delta(h, -h) - \Delta(-h, -h) - 4\Delta(-h, 0) \\ &\quad - \Delta(-h, h)] - \frac{h^2}{6} \frac{\partial}{\partial x} \left( \frac{\partial^2 \Delta}{\partial x^2} + \frac{\partial^2 \Delta}{\partial y^2} \right) \Big|_{(0,0)} \\ &\quad - \frac{h^4}{72} \frac{\partial}{\partial x} \left( \frac{\partial^4 \Delta}{\partial x^4} + 2 \frac{\partial^4 \Delta}{\partial x^2 \partial y^2} + \frac{\partial^4 \Delta}{\partial y^4} \right) \Big|_{(0,0)} - \frac{h^4}{180} \frac{\partial^5 \Delta}{\partial x^5} \Big|_{(0,0)} + O(h^5) \end{aligned} \quad (24)$$

$$\begin{aligned} \frac{\partial \Delta}{\partial y} \Big|_{(0,0)} &= \frac{1}{12h} [\Delta(-h, h) + 4\Delta(0, h) + \Delta(h, h) - \Delta(h, -h) - 4\Delta(0, -h) \\ &\quad - \Delta(-h, -h)] - \frac{h^2}{6} \frac{\partial}{\partial y} \left( \frac{\partial^2 \Delta}{\partial x^2} + \frac{\partial^2 \Delta}{\partial y^2} \right) \Big|_{(0,0)} \\ &\quad - \frac{h^4}{72} \frac{\partial}{\partial y} \left( \frac{\partial^4 \Delta}{\partial y^4} + 2 \frac{\partial^4 \Delta}{\partial x^2 \partial y^2} + \frac{\partial^4 \Delta}{\partial x^4} \right) \Big|_{(0,0)} - \frac{h^4}{180} \frac{\partial^5 \Delta}{\partial y^5} \Big|_{(0,0)} + O(h^5) \end{aligned} \quad (25)$$





results section, the accuracy of the isotropic discretization for the color gradient is compared to the standard second order anisotropic color gradient. The use of the isotropic discretization for the color gradient led to a significant increase in the accuracy of the model.

#### 2.4. Setting the surface tension

Following a theoretical development from Ref. [22] and his predecessors [5], it is possible to predict the surface tension between the two fluids using only the basic parameters of the model. Knowing the form of the expression describing the surface tension and performing simulations on planar interfaces, as in Refs. [4,22], a function of  $\rho_r$ ,  $\gamma$ ,  $\omega$ ,  $A_r$ , and  $A_b$  can be determined to approximately describe the surface tension. In this work, different color gradient approximations are used and, depending on which is selected, the surface tension is set in a slightly different way. When the second order anisotropic color gradient is used,  $\vec{F}_I$ , the surface tension is adjusted by combining the model parameters, as follows [4]:

$$\sigma_{ani} = \frac{4}{3} \frac{\left(1 + \frac{1}{\gamma}\right) \frac{\rho_r}{2}}{\omega} (A_r + A_b) \quad (36)$$

A similar expression is used for the second  $\vec{F}_{II}$ , fourth  $\vec{F}_{III}$ , and sixth order  $\vec{F}_{IV}$  isotropic color gradient. The surface tension is also adjusted in a same way, but with a different multiplicative constant:

$$\sigma_{iso} = \frac{2}{9} \frac{\left(1 + \frac{1}{\gamma}\right) \frac{\rho_r}{2}}{\omega} (A_r + A_b) \quad (37)$$

#### 2.5. Incompressible limit of the model

The current model exploits the possibility of using different speeds of sound in each phase. It is known that the value of  $\sqrt{1/3}$  for the speed of sound in the LBM is only one possibility, and that it is only the most common one [40]. The speed of sound in the LBM is set by the value of the rest lattice weight  $\alpha_k$  [41]. Different speeds of sound mean that the Navier–Stokes equations are recovered in each phase with their own speed of sound. Moreover, and most importantly, at the interface, Reis and Phillips have shown that the equations for two-phase flows are also recovered [22]. It is by exploiting the fact that different speeds of sound can be taken in each phase that the RK model can simulate the density ratios between the phases [9].

Now let us look at the incompressible condition of the LBM in the context of this model. Because the speed of sound in the high-density phase (red fluid in our model) is lower than in the low-density phase, the maximum possible Mach number,  $M_{max}$ , in the flow at each position in the computational domain is approximately equal to:

$$M_{max} \approx \frac{|\vec{u}|}{c_s^r} \quad (38)$$

To verify the incompressible limit, we want to keep a small Mach number, let's say smaller than 0.1. This leads to the following constraint:

$$|\vec{u}| \leq (0.1)c_s^r \quad (39)$$

Eq. (11) then gives:

$$|\vec{u}| \leq (0.1)\sqrt{3/5(1 - \alpha_r)} \quad (40)$$

Finally, Eq. (10) gives:

$$|\vec{u}| \leq (0.1) \frac{\sqrt{3/5(1 - \alpha_b)}}{\sqrt{\gamma}} \quad (41)$$

For the light phase, as low a value of  $\alpha_b$  as possible, is always chosen to help the incompressible limit constraint of the red phase. In this paper, we chose  $\alpha_b = 0.2$ . It is then found that, in the LB unit system, maximum velocity is inversely proportional to the square root of the density ratio. Because of the square root, the constraint is not as limiting as might be expected, and further research may one day remove it altogether. When the density ratio is high, it is important to respect the constraint in Eq. (41). In this paper, when the results are accurate, the incompressible limit of the LBM is respected.

### 3. Numerical results

The focus of the numerical simulations is on the circular steady bubble, because it is the best test case for evaluating the isotropy of the numerical scheme. In this section, we concentrate on a steady (red) bubble of radius  $R$  immersed in a different (blue) fluid.

Only calculations aimed at stationary solutions are performed here, so it is convenient to introduce the stopping criterion common to all simulations:

$$\max_{\text{all distribution functions}} \left\{ |(N_i^k)^{(n)} - (N_i^k)^{(n-1)}| \right\} \leq \epsilon \quad (42)$$

with  $\epsilon = 10^{-9}$  and  $n$  denoting the time step number. This condition is only checked every 2000 time steps, in order to reduce the computational cost. Under this criterion, all the numerically stable simulations performed in this paper converge in a finite number of time steps. Even though this criterion is rigorous, it does not necessarily guarantee that all solutions will be fully steady. However, all the numerically stable simulations converge to results that represent the steady state solutions well. The number of time steps required to converge the solution to such a small value of  $\epsilon$  could be high, and, because many numerical simulations were undertaken, the computational cost limited the choice for  $\epsilon$ .

Some input parameters are the same for all numerical simulations, and these are listed in Table 3. We can see that, depending on  $\gamma$ , the value of  $\alpha_r$  is found from Eq. (10). The value for  $\alpha_k$  should normally be chosen to obtain the standard weight (4/9) when the density ratio is unity. However, in our particular case, to compare the overall trend for many density ratios, it is better to choose the same  $\alpha_b$  for all simulations. Therefore, we chose a value of  $\alpha_b = 0.2$  that is not too high, to help reduce the incompressible LBM constraint in the red, higher density phase (Eq. (41)).

The free parameter  $\delta$  does not influence the solution, because only the unit viscosity ratio is simulated. The decision to choose fluid viscosities that will yield a unit relaxation time was made for simplicity. Note that  $\omega = 1$  is not necessarily the most accurate.

#### 3.1. Steady bubble: Laplace's law

The aim of this subsection is to verify whether or not the surface tensions of the model predicted by Eqs. (36) and (37) are consistent with Laplace's law [39,22]:

$$\sigma_{Laplace} = R\Delta p \quad (43)$$

where  $\Delta p = p_{in} - p_{out}$  is the pressure jump across the inside and outside of the bubble. The pressures of the bubble, inside  $p_{in}$  and outside  $p_{out}$ , are measured as follows:

**Table 3**  
Constant input parameters for all simulations.

$\alpha_b$	$\delta$	$v_r$	$v_b$
0.2	0.1	1/6	1/6

$$p_{in} = p_{in}^r + p_{in}^b = \frac{3}{5} \rho_{r,in} (1 - \alpha_r) + \frac{3}{5} \rho_{b,in} (1 - \alpha_b) \quad (44)$$

$$p_{out} = p_{out}^r + p_{out}^b = \frac{3}{5} \rho_{r,out} (1 - \alpha_r) + \frac{3}{5} \rho_{b,out} (1 - \alpha_b)$$

with

$$\begin{aligned} \rho_{r,in} &= \langle \{\rho_r | \psi \geq 0.999999\} \rangle \\ \rho_{b,in} &= \langle \{\rho_b | \psi \geq 0.999999\} \rangle \\ \rho_{r,out} &= \langle \{\rho_r | \psi \leq -0.999999\} \rangle \\ \rho_{b,out} &= \langle \{\rho_b | \psi \leq -0.999999\} \rangle \end{aligned} \quad (45)$$

where the symbol  $\langle \cdot \rangle$  stands for the average.

In a previous work [4], the internal and external pressures were computed for each fluid separately in the single fluid regions considered. That is to say, the internal and external pressure calculations were performed using only the red and blue fluids respectively. According to the numerical model, the more consistent, easier, and more robust method is to compute the pressure by including the pressure contributions of both fluids, even if these are small on regions where one of them is fully predominant.

For these simulations, the computational domain is discretized with a lattice of  $128 \times 128$  sites geometrically located over the computational domain  $[1, 128] \times [1, 128]$ . Initially, the red fluid is placed at a distance of at most  $R$  from the center of the computational domain  $((x - 64.5)^2 + (y - 64.5)^2 \leq R^2)$ . The fluid is initialized with zero velocity equilibrium distribution functions. For the blue fluid, the field is initialized in the same way. Periodic boundary conditions are used at the four ends of the computational domain. Depending on the color gradient, the parameters  $A_r = A_b$  are obtained from Eqs. (36) or (37) and by using the surface tension  $\sigma_{ani}$  or  $\sigma_{iso}$ , and the other three parameters  $\rho_r$ ,  $\gamma$ , and  $\omega$ .

A total of 674 simulations were selected to study how the various parameters in the current model influence the accuracy of the results. This is the number of all the possible combinations of input parameters, i.e.  $674 = 4 \times 7 \times 2 \times 3 \times 3 \times 1 + 4 \times 7 \times 2 \times 3 \times 1 \times 1$ . Tables 4 and 5 summarize these combinations.

Below, the superscript  $i$  indicates a quantity obtained at the end of the  $i$ th simulation. Let us denote by:

$$E_i^i = 100 \frac{|\sigma_{Laplace}^i - \sigma_{ani}^i|}{\sigma_{ani}^i} \quad (46)$$

the relative error, as a percentage, between the surface tension  $\sigma_{ani}$  and  $\sigma_{Laplace}^i$ , with  $\sigma_{ani}$  as a reference when the simulation is performed with the anisotropic color gradient  $\vec{F}_I$ . Similarly, when the simulation is performed with the isotropic color gradients  $\vec{F}_{II}$ ,  $\vec{F}_{III}$ , or  $\vec{F}_{IV}$ , the relative error is denoted  $E_{II}^i$ ,  $E_{III}^i$ , or  $E_{IV}^i$ , but with  $\sigma_{iso}$  used as reference.

For a density ratio  $\gamma = 1$ , Fig. 3 shows the relative error as a function of the surface tension resulting from the various simulations listed in Table 4. In the same way, Figs. 4 and 5 show the relative errors for  $\gamma = 100$  and  $\gamma = 1000$  respectively. For a clear reading of the results presented in these figures, the plot convention must

**Table 5**

Some combinations of parameters for the steady bubble simulations.

Color gradient	$\sigma_{ani} = \sigma_{iso}$	$R$	$\rho_r$	$\gamma$	$\beta$
$\vec{F}_I$	$10^{-2}$	20	0.2	1000	0.7
$\vec{F}_{II}$	$10^{-3}$	30	1		
$\vec{F}_{III}$	$10^{-4}$		5		
$\vec{F}_{IV}$	$10^{-5}$				
	$10^{-6}$				
	$10^{-7}$				
	$10^{-8}$				

be explained: The axes are on a log–log scale. From left to right, they show the results obtained from the second order anisotropic gradient, second order isotropic gradient, fourth order isotropic gradient, and sixth order isotropic gradient. On each of these plots, there are four lines, each of them corresponding to a “linear best fit” obtained from the simulation results of a particular color gradient. This allows a better appreciation and comparison of the general behavior of the error as a function of surface tension for each of the four color gradients. The figures can be more easily understood when they are represented in color (available online), because the “best fit lines” are the same color as the points they fit. The line style specifiers used to associate the best fit lines with the color gradient are shown in Fig. 2.

The results displayed in Fig. 3 merit a few comments. First, for  $\gamma = 1$ , the gradient  $\vec{F}_I$  leads to accurate and valid results only for a high surface tension. When low surface tensions are simulated, the gradient approximation  $\vec{F}_I$  yields inaccuracy, represented by a non circular bubble at steady state. Further details of this behavior are given in the next subsection. In general, all isotropic gradient discretizations lead to more accurate results than the anisotropic gradient over all the surface tensions in the spectrum that were simulated, i.e.  $O(10^{-2})$  to  $O(10^{-8})$ . Surprisingly, with the second order isotropic gradient, the results are more accurate, on average, than with the fourth and sixth order isotropic gradients. This strange behavior is found in the error for the surface tension plot only (Fig. 3), and not in the spurious currents plot (Fig. 9). It is important to keep in mind the way the inside pressure and outside pressure of the bubble are measured. The way to do this is heuristic (Eq. (44)), which may have something to do with the observed behavior. We can only have full confidence in the surface tension errors when we look at the results on average, i.e. by looking at the overall trend of all 674 simulations. The tendency clearly shows improvement for the surface tension with an isotropic color gradient versus the original anisotropic discretization. Also note that the results for the spurious currents are more reliable, because their measurement is not heuristic, and this confirms the same trend in behavior. Nevertheless, we would have expected that the higher order gradients would always perform better than the lower order gradients. However, gradient-order effects are expected to be much more significant as the grid is refined, and better results could be expected on a fine grid with a higher order gradient. At least it can be said that the lower the surface tension, the better the precision (less scatter) with the higher order gradients. Results for the fourth and sixth order isotropic gradients are practically the same, with an error that is always less than 1%.

For  $\gamma = 100$  in Fig. 4, the second order anisotropic gradient still leads to the worst results on average. An important fact to note is that, when increasing the density ratio to  $O(100)$ , the two second



**Fig. 2.** Line style specifiers associated with the color gradient.

**Table 4**

Some combinations of parameters for the steady bubble simulations.

Color gradient	$\sigma_{ani} = \sigma_{iso}$	$R$	$\rho_r$	$\gamma$	$\beta$
$\vec{F}_I$	$10^{-2}$	20	0.2	1	0.99
$\vec{F}_{II}$	$10^{-3}$	30	1	100	
$\vec{F}_{III}$	$10^{-4}$		5	1000	
$\vec{F}_{IV}$	$10^{-5}$				
	$10^{-6}$				
	$10^{-7}$				
	$10^{-8}$				

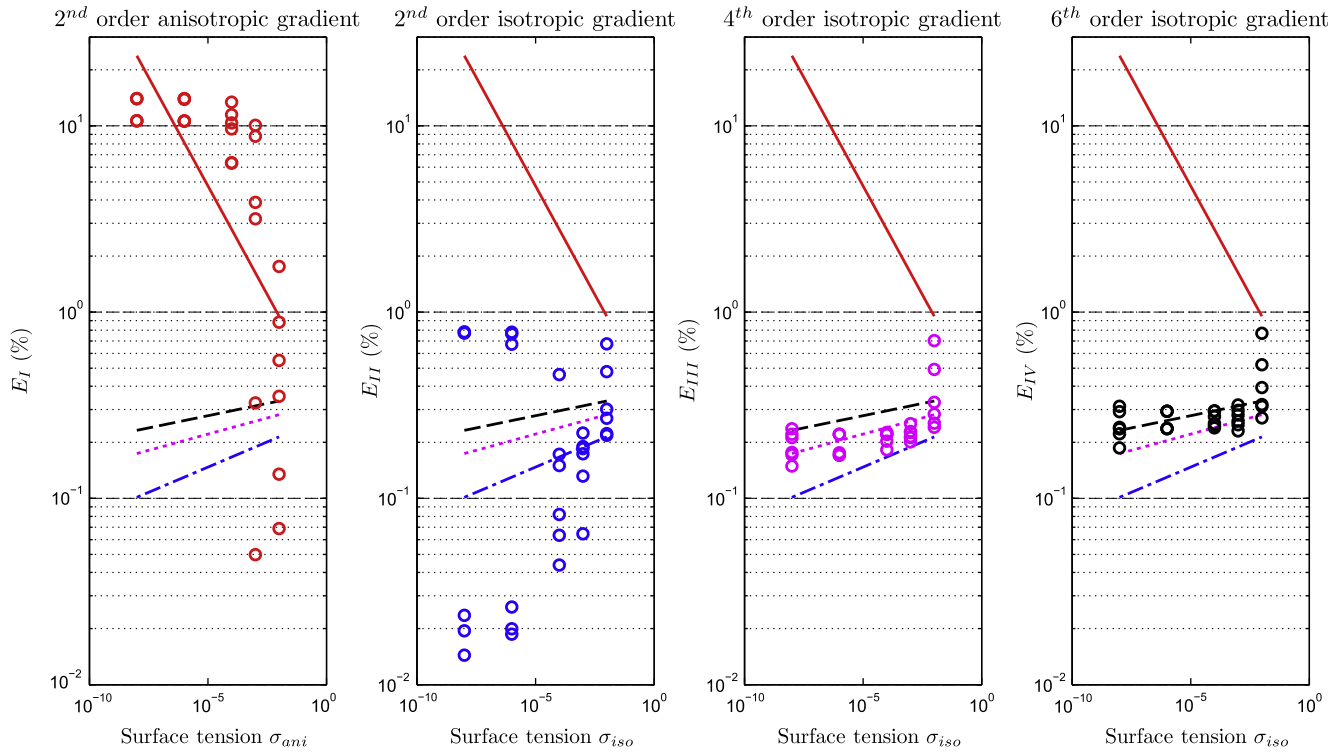


**Fig. 3.** Steady bubble: relative error with the Laplace surface tension as a function of surface tension ( $\gamma = 1$  and  $\beta = 0.99$ ).

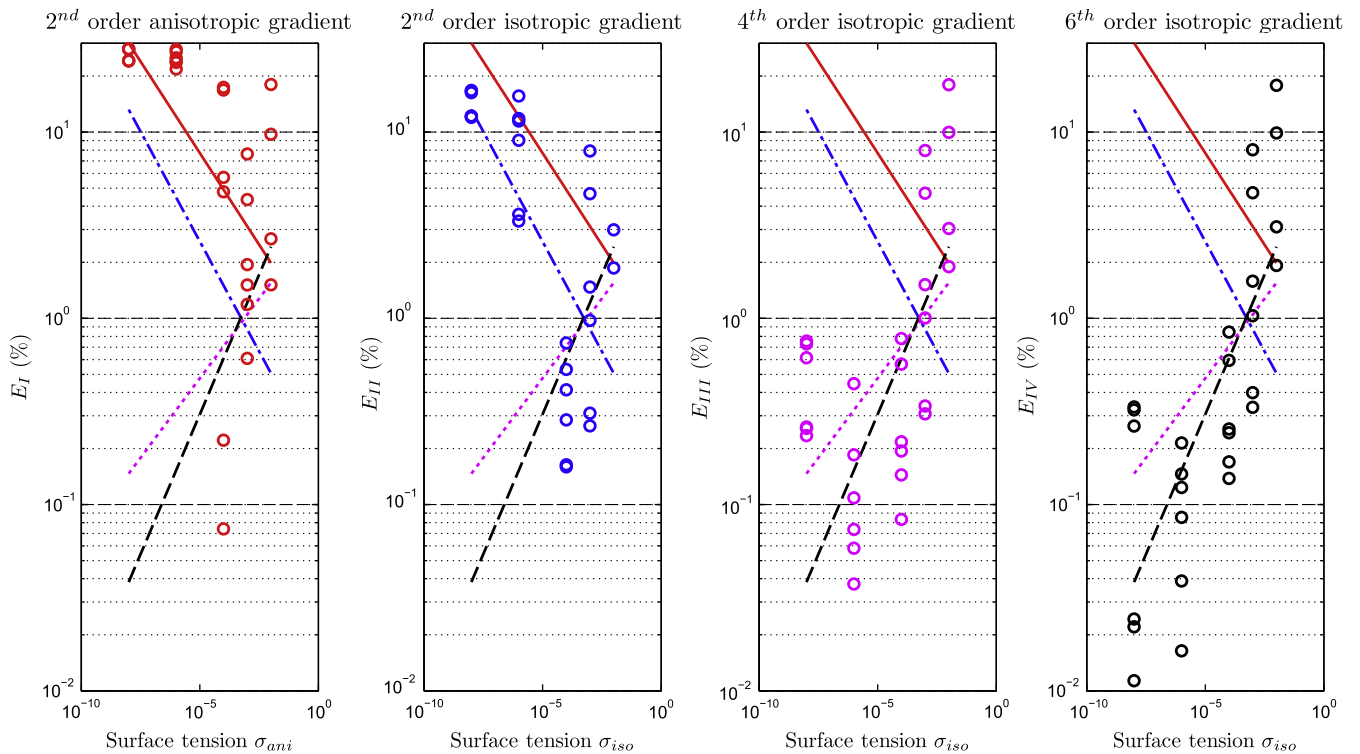


**Fig. 4.** Steady bubble: relative error with the Laplace surface tension as a function of surface tension ( $\gamma = 100$  and  $\beta = 0.99$ ).

order gradient discretizations, both the isotropic and anisotropic, behave in the same way when the surface tension is low, i.e. the results are less accurate, or are inaccurate. This again can be explained by the deformation of the bubble shape. For the fourth order and sixth order isotropic gradients, the results are still similar,

but the sixth order gradient starts to produce more accurate results in the low surface tension regime. This difference increases when the density ratio climbs to  $O(1000)$ . We need to point out that 10 of the simulations with  $\gamma = 100$  were unstable in the  $O(10^{-2})$  surface tension regime, and that this instability affects all four color



gradients. To avoid distorting the pattern of the best fit lines, all simulations with  $\sigma = 10^{-2}$  have been removed from Fig. 4.

For  $\gamma = 1000$  in Fig. 5 and for the  $O(10^{-2})$  and  $O(10^{-3})$  surface tension regimes, 29 simulations among the four color gradients were unstable. As a result, all the simulations with  $\sigma = 10^{-2}$  and  $\sigma = 10^{-3}$  have been removed from Fig. 5. Overall, these simulations were unstable because the incompressible limit of the LBM was not respected. The spurious currents were too high and pulled in a high, non physical Mach number, which renders the simulation unstable. The results obtained for the two second order gradients were shown to be very similar to those of the previous case with  $\gamma = 100$ . These two gradients lacked sufficient isotropy to accurately simulate a low surface tension with a large density ratio. Looking at Fig. 5 for  $\sigma = 10^{-4}$ , it can be seen that the results are practically the same for all the isotropic gradients, and, as surface tension decreases, the higher order isotropic gradient always performs better than the second order isotropic gradient. With these model parameters, it also appears that the isotropy of the fourth and sixth order isotropic gradients is not sufficient to simulate the steady bubble accurately when the surface tension is very low,  $O(10^{-7})$  or  $O(10^{-8})$ , as, at this limit, the error was found to be high for some simulations. Nevertheless, we can note that the sixth order isotropic gradient performs better than the fourth order one for a low surface tension.

To be able to accurately simulate very low surface tension with a large density ratio such as  $O(1000)$ , we can adjust the thickness of the interface to reduce the errors of the gradient discretization. By changing the parameter  $\beta$  from 0.99 to 0.7, the thickness of the interface increases slightly and the results become much more accurate. We can see from the simulation results of Table 5 shown in Fig. 6 that, for a density ratio of  $O(1000)$  and for surface tensions from  $O(10^{-8})$  to  $O(10^{-4})$ , the error with the Laplace surface tension is almost always less than 1% when the fourth or sixth order isotropic gradients are used. It might be possible, if the problem is well

posed and not subject to numerical round-off error accumulation, to accurately simulate even lower surface tension, but this has not been tested. Also, it might be possible to use a higher value than 0.7 for  $\beta$  to achieve similar accuracy; however, this has not been tested either. Moreover, we note that the outcome of the two second order gradients, both isotropic and anisotropic, is unsatisfactory.

Overall, the above results can be summarized as follows. As the surface tension decreases, the error becomes smaller with an increase in the interface thickness and in the isotropy of the color gradient. This behavior becomes increasingly strong as the ratio of the density of the two fluids increases. In short, the interface thickness and the isotropy of the color gradient are two key factors required to accurately simulate large density ratios for a wide range of surface tensions. We must be careful to select an interface thickness that is not too large, because the numerical position of the interface may differ greatly from the true physical one.

### 3.2. Steady bubble: bubble deformation

In this subsection, four numerical simulations illustrate the reason why large errors are found when the second order isotropic or anisotropic color gradients are used with a low surface tension. In these simulations, the surface tension is set to  $10^{-6}$ , also  $\rho_r = 1$ ,  $R = 30$ ,  $\beta = 0.99$ , and  $\gamma = 10$ . For each of the four color gradients, a snapshot of the color field  $\psi$  at steady state is shown in Fig. 7. The error with the Laplace surface tension obtained at steady state and the number of time steps needed to reach steady state are also listed in Table 6.

Looking at Fig. 7, it seems clear that the errors from Table 6 are mainly due to bubble deformation. The results obtained with the second order isotropic gradient are better than the diamond shaped bubble obtained with the second order anisotropic gradient. Note that the accuracy and the bubble shape obtained at

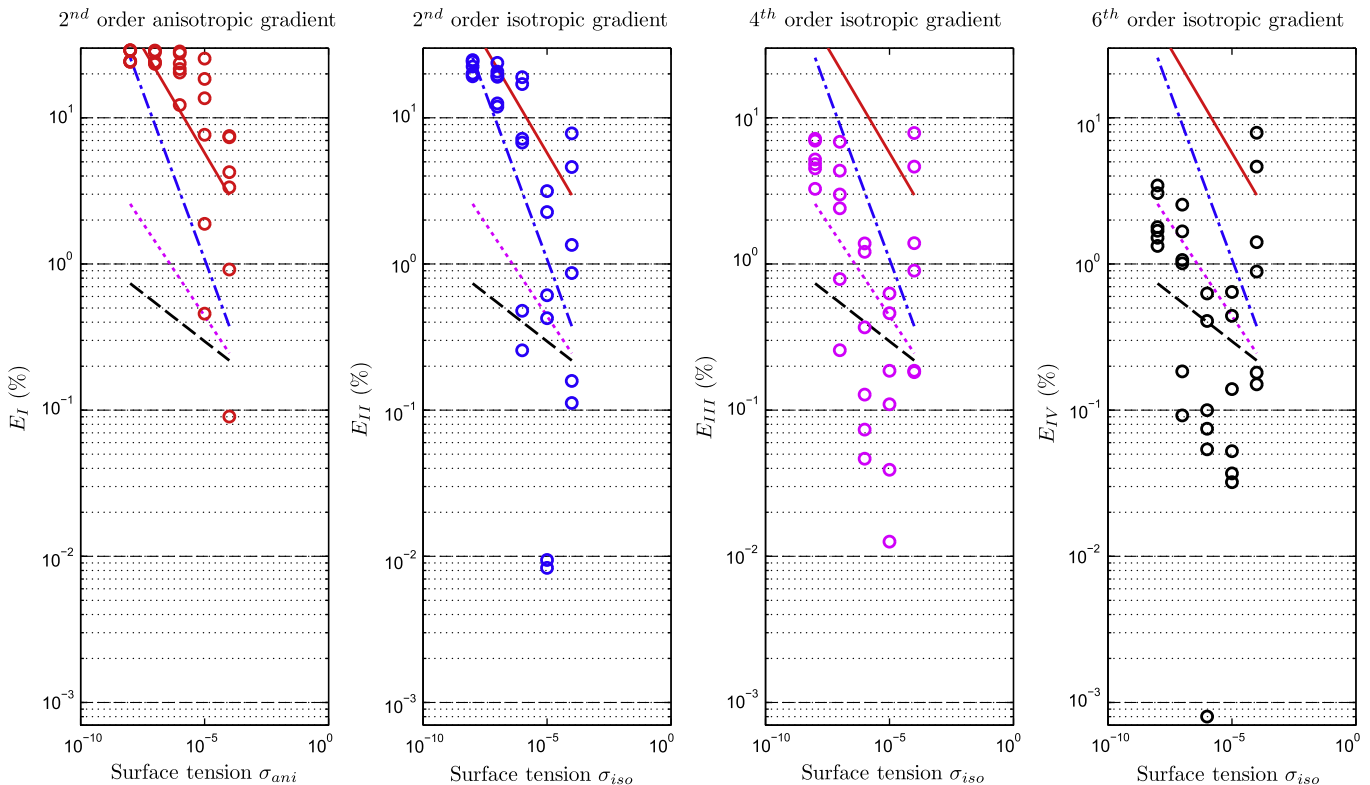
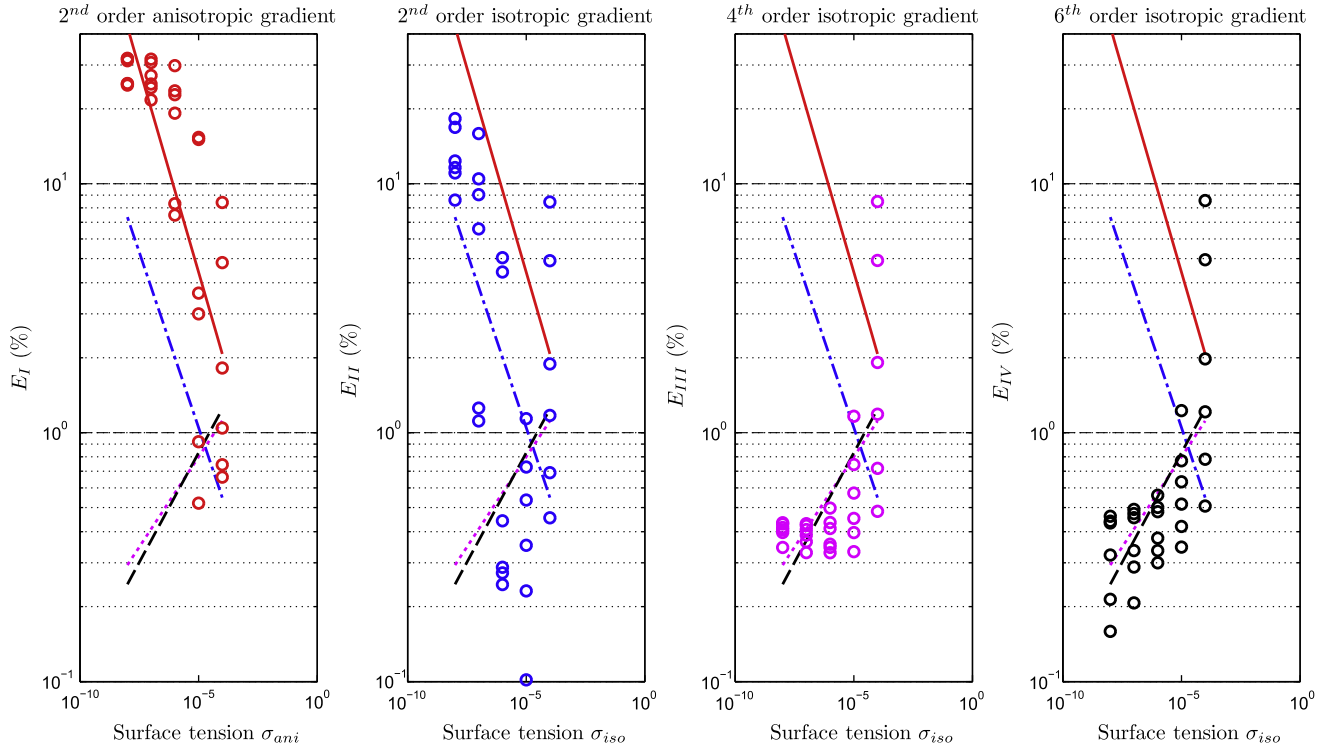
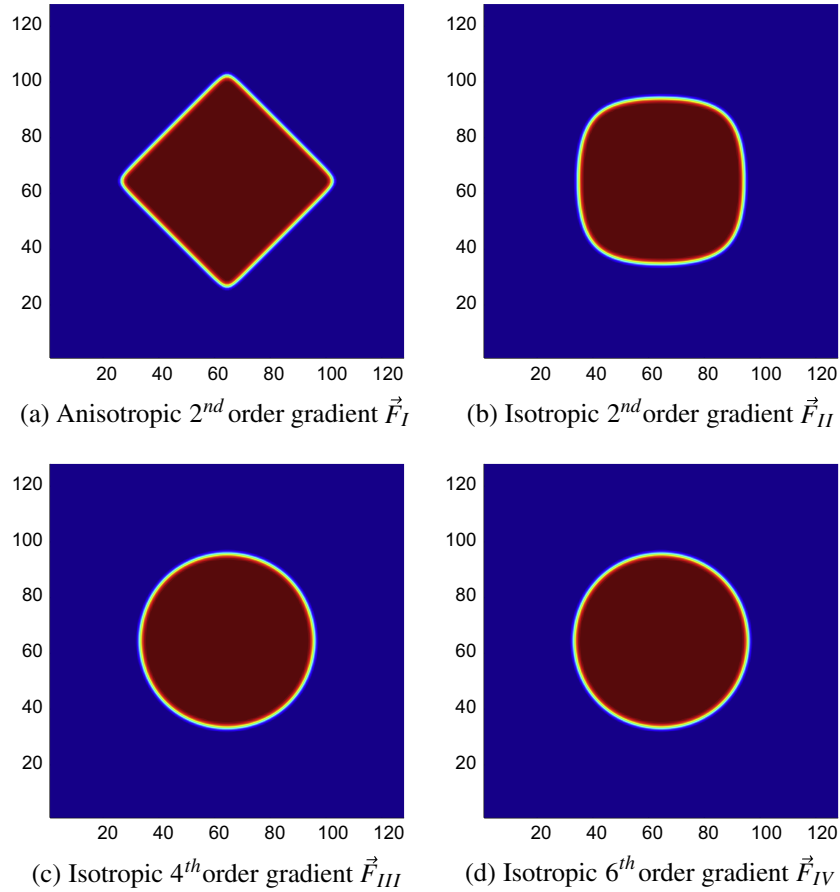


Fig. 5. Steady bubble: relative error with the Laplace surface tension as a function of surface tension ( $\gamma = 1000$  and  $\beta = 0.99$ ).



**Fig. 6.** Steady bubble: relative error with the Laplace surface tension as a function of surface tension ( $\gamma = 1000$  and  $\beta = 0.7$ ).



**Fig. 7.** Bubble shape at steady state for different color gradients ( $\gamma = 10$ ).

steady state are much better with the higher order isotropic color gradient for this case. Since the bubble is deformed significantly with  $\vec{F}_{II}$  and  $\gamma$  is relatively small, one conclusion is that the isotropy of this gradient is not sufficient to produce accurate results for a low surface tension and a high-density ratio.

When the surface tension is low, the effect of the gradient discretization errors may be of the same order as the effect of the cohesive force between the molecules, which is introduced by the perturbation operator to minimize the contact area between the two fluids. Note that more mass is added in the direction normal to the interface when perturbation is high. When the discretization errors generated by the gradient anisotropy are too large, the cohesive forces may not be able to maintain a minimal contact area. In other words, when using high order isotropic

discretization, the effects of the errors arising from anisotropic discretization are probably less than the effects of the forces of cohesion, or at least not high enough to significantly deform the bubble. Similarly, when perturbation is low, the mass added in the direction normal to the interface cannot counter the effect of the accumulation of directionally biased discretization errors. This reasoning may explain, at least in part, the bubble deformation at low surface tension, along with the poor accuracy.

Spurious currents constitute another factor that needs to be taken into account, as they may also deform the bubble, although the anisotropic discretization error is probably the main cause of inaccuracy. The interface deformation may not be occurring primarily because of the effect of the velocity  $\vec{u}$  in the equilibrium distribution of the single-phase collision operator, but rather because of the anisotropic forces, caused by anisotropic discretization, that are present in the perturbation and recoloring operator. It is thought that this is the main problem, because, with a higher order isotropic color gradient, the approximation of the color gradient is better and the bubble deformation disappears. Spurious currents could also come from an anisotropic discretization of the Boltzmann equation. Therefore, spurious currents seem to be a problem caused by anisotropy. Naturally, spurious currents are extremely

**Table 6**  
Surface tension errors and time step number at steady state.

	$\vec{F}_I$	$\vec{F}_{II}$	$\vec{F}_{III}$	$\vec{F}_{IV}$
$E_X$ (%)	24.31	1.639	0.207	0.239
$t_{end}$	190,000	1,808,000	1,096,000	1,028,000

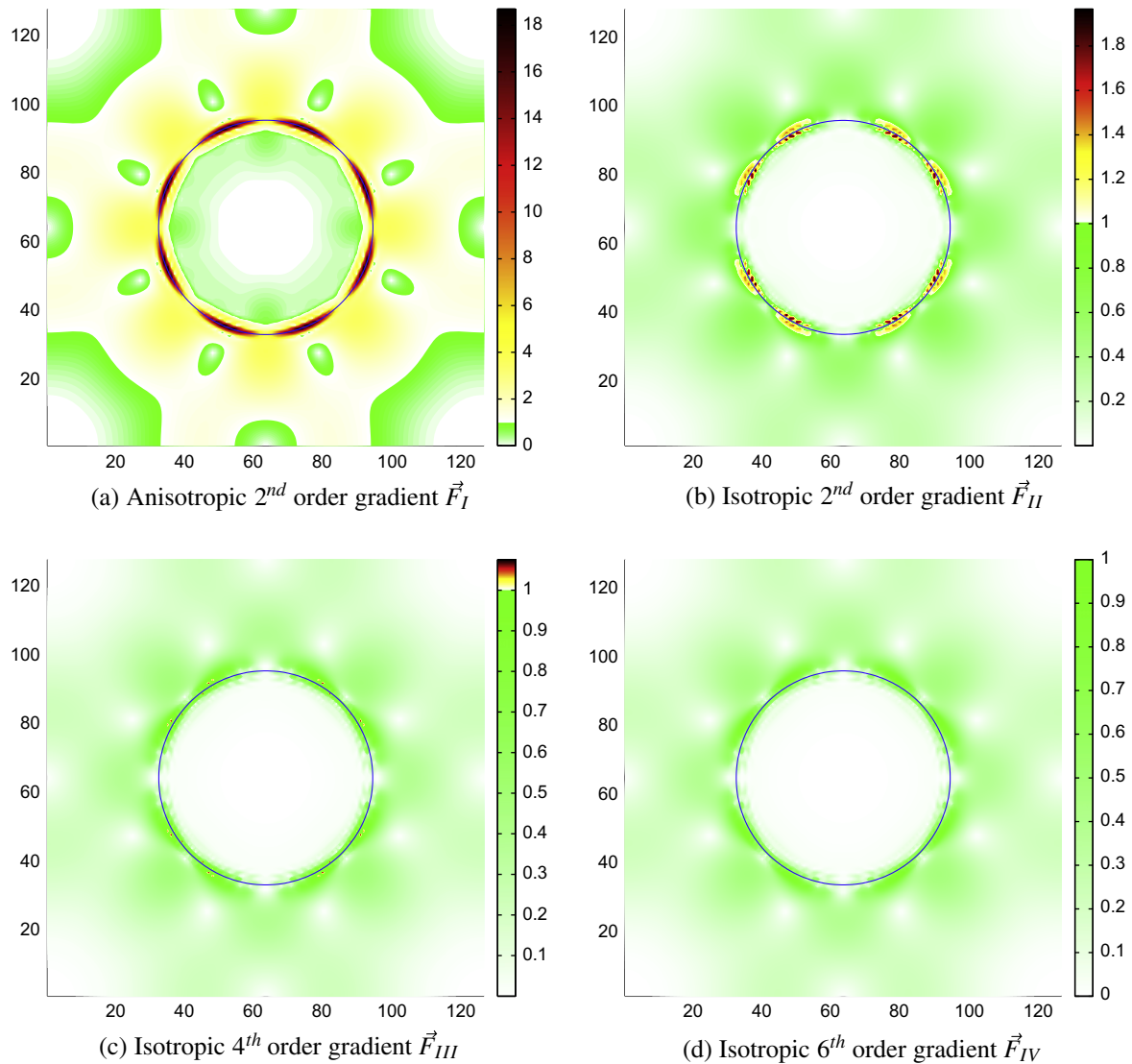


**Fig. 8.** Spurious currents at steady state obtained from different color gradient ( $\gamma = 10$ ).

important to numerical stability, as higher ones directly increase the Mach number in a non physical way. From this perspective, we can understand why high order isotropic color gradients are better at simulating fluids with a low surface tension.

Generally, the fourth order isotropic color gradient will be a better choice, for two reasons. The first is obvious: the bubble shape and accuracy at steady state are usually better. The second is less so: the bubble deformation with  $F_{II}$  happens very slowly, and therefore

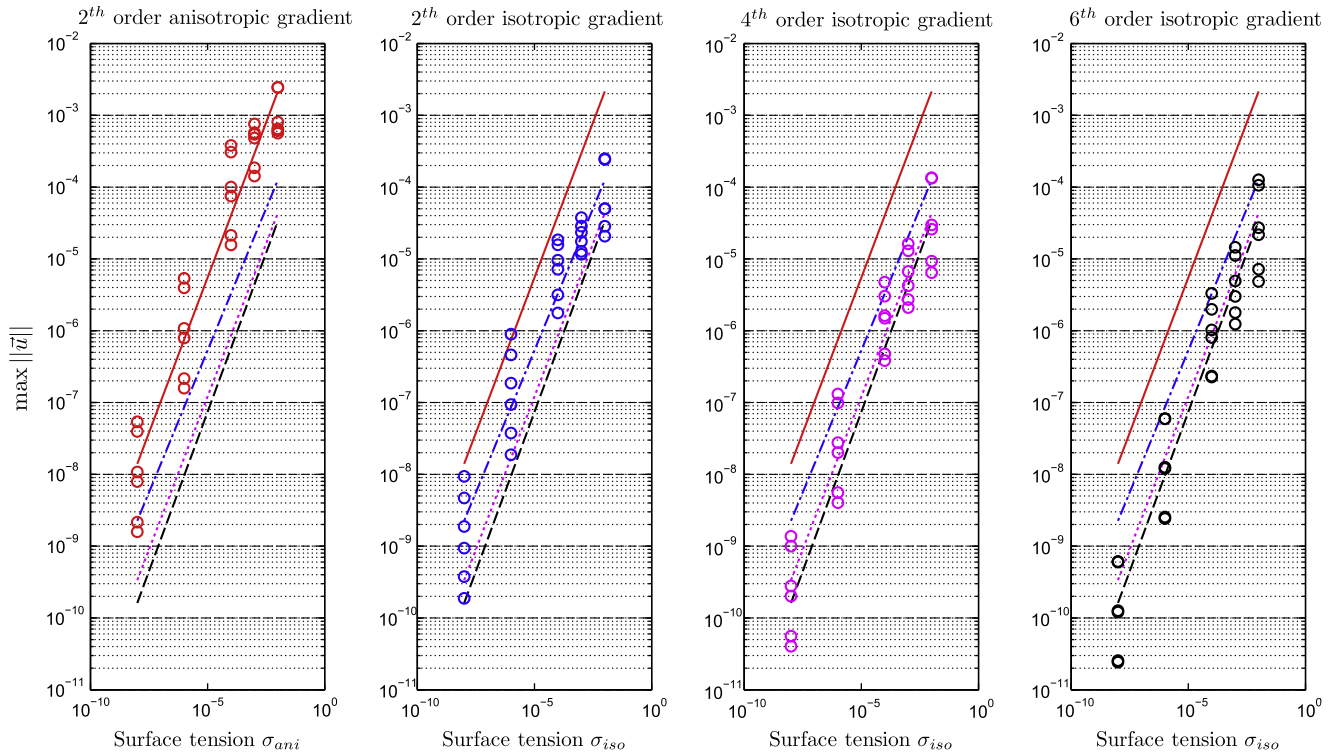


Fig. 9. Maximum velocity magnitude as a function of the surface tension resulting from the various simulations of the steady bubble ( $\gamma = 1$  and  $\beta = 0.99$ ).

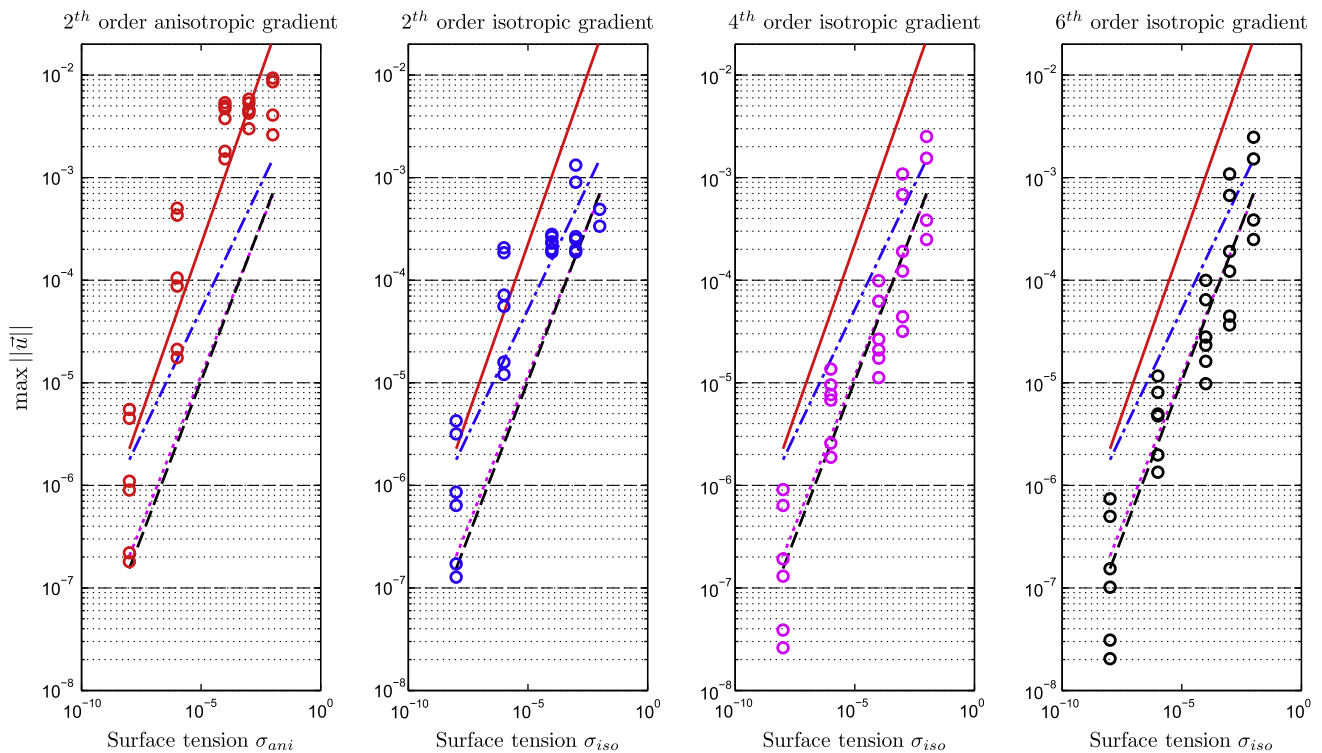


Fig. 10. Maximum velocity magnitude as a function of the surface tension resulting from the various simulations of the steady bubble ( $\gamma = 100$  and  $\beta = 0.99$ ).

causes the simulation to reach steady state with many more time steps than with the fourth order isotropic gradient  $F_{III}$  (Table 6). Even though  $F_{III}$  costs more to calculate than  $F_{II}$ , because some

neighbors of neighbors are involved in calculating  $F_{III}$ , the total simulation time is usually less with  $F_{III}$ , owing to the smaller number of time steps needed to reach steady state (almost half, in this case).

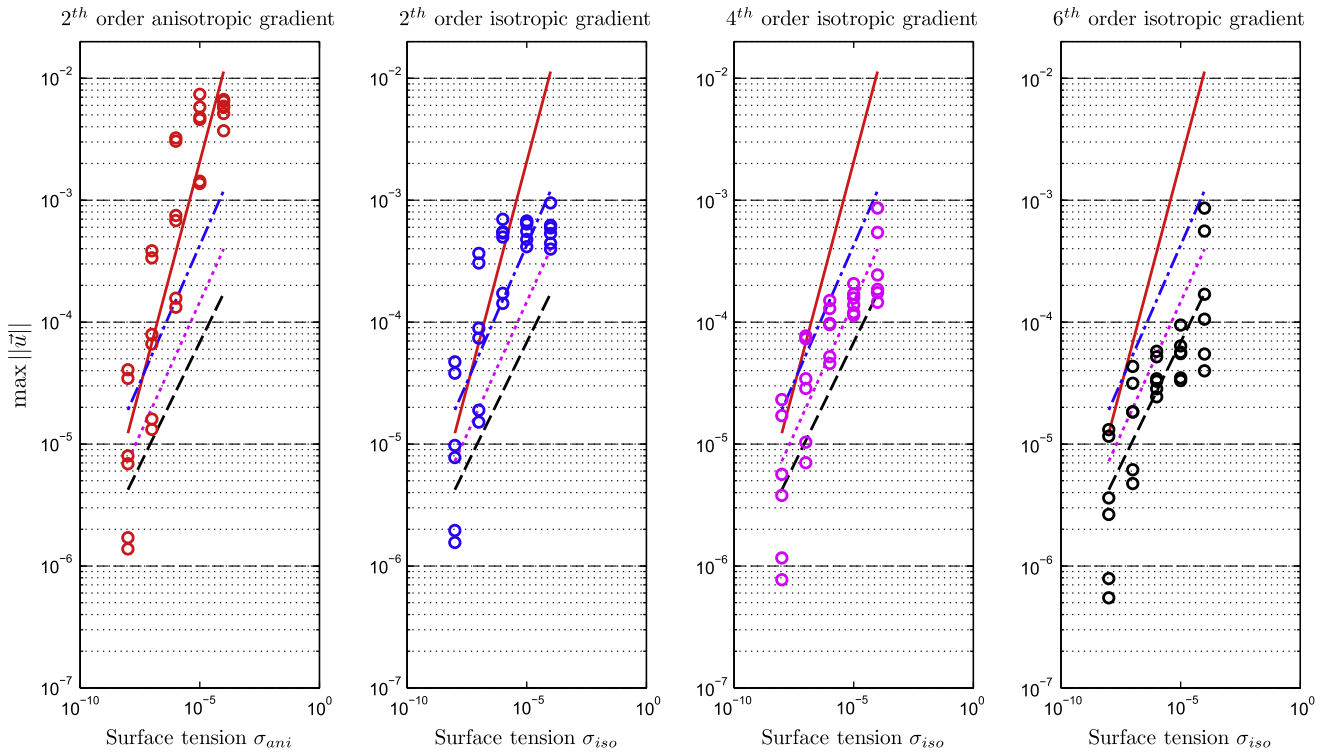


Fig. 11. Maximum velocity magnitude as a function of the surface tension resulting from the various simulations of the steady bubble ( $\gamma = 1000$  and  $\beta = 0.99$ ).

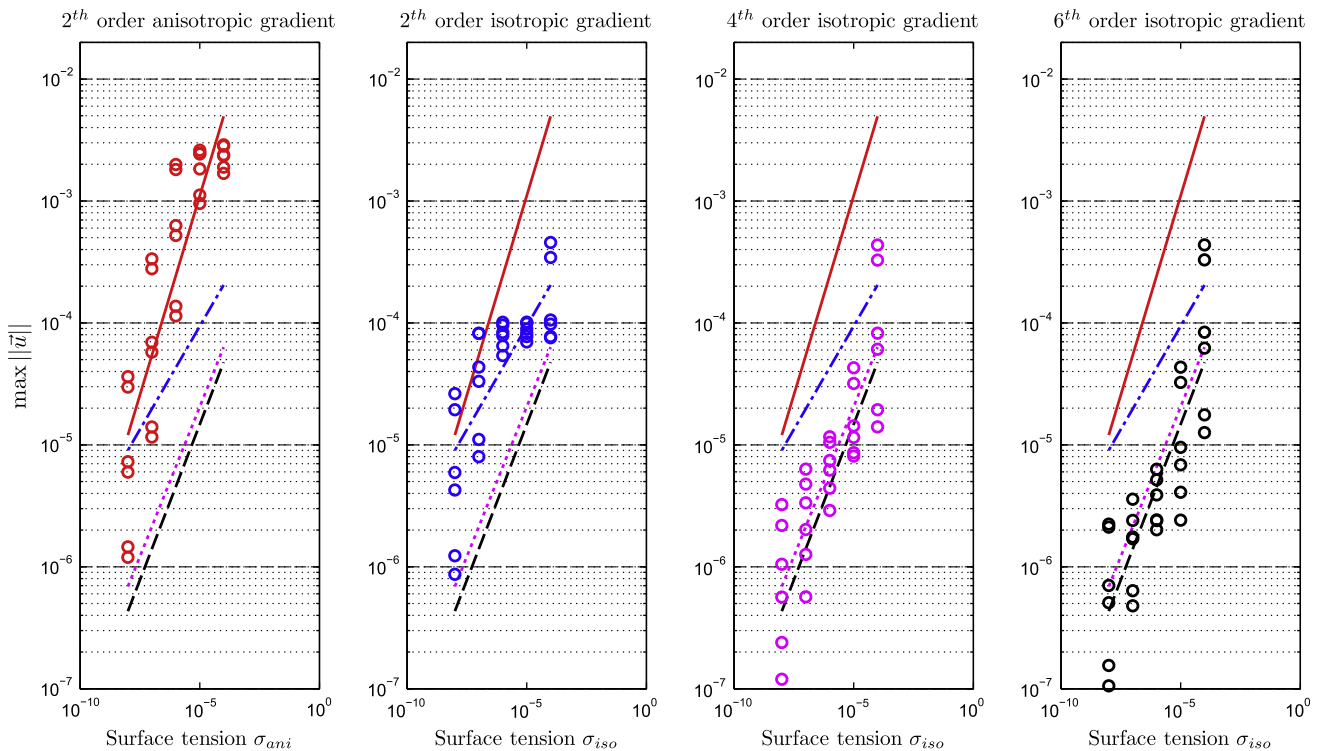


Fig. 12. Maximum velocity magnitude as a function of the surface tension resulting from the various simulations of the steady bubble ( $\gamma = 1000$  and  $\beta = 0.7$ ).



### 3.3. Steady bubble: spurious currents

First, we illustrate the problem of spurious currents with four numerical simulations. The surface tension,  $\sigma$ , is set to  $10^{-2}$ , also  $\rho_r = 1$ ,  $R = 30$ ,  $\beta = 0.99$ , and  $\gamma = 10$ . For each of the four color gradients, a snapshot of the velocity magnitude field at steady state is shown in Fig. 8. (Color is available online, and is needed to fully appreciate these snapshots.) For each of the four plots, the velocity magnitude is scaled using the maximum velocity over the computational domain that was obtained at steady state from the simulation performed with the sixth order isotropic gradient. This makes it easier to compare the color gradients in terms of the magnitude of the spurious currents. The color bar is therefore scaled with two color “spectra”. In order to illustrate a velocity less than the maximum obtained with the sixth order isotropic gradient, the first color of the spectrum goes from white to green to represent a velocity ratio from 0 to 1. If the velocity ratio is greater than 1, then a second color spectrum is used that goes from white, to yellow, to red, to black, where black represents the magnitude of the maximum velocity of the current simulation. The bubble shape is also plotted over the velocity magnitude field. An important feature of the bubble shape, because surface tension is high, is that it is circular at steady state for all gradient discretizations.

Looking at the color bar in Fig. 8a and b, we can see that the spurious currents are reduced by one order of magnitude ( $\approx 18/1.8$ )

when the second order isotropic gradient is used instead of the second order anisotropic gradient. This result is very similar to the findings of [33,36] with the FE and SC methods. As did Halliday et al. in [5], we found that the spurious currents are strongest at the interface.

It is also important to note that a significant, but not very large, reduction in the spurious currents is achieved using the fourth order isotropic gradient instead of the second order isotropic gradient. Between the fourth and sixth order gradient, there is almost no reduction in spurious currents. It seems, therefore, that the fourth order isotropic gradient is worth the cost for these cases versus the second order isotropic gradient. Here, the sixth order isotropic gradient has not been shown to be worth applying when its results are compared with those obtained with the fourth order isotropic gradient.

Figs. 9–11 show the maximum velocity magnitude at steady state as a function of the surface tension in the same way as the relative error is shown as a function of the surface tension in Figs. 3–5. Again, these plots are drawn using the simulation results obtained with the various input parameters in Table 4, which provides a much better overview of the spurious currents as a function of the model parameters.

From Fig. 9, we can note that, for  $\gamma = 1$ , the intensity of the spurious currents is linearly proportional to the surface tension. This suggests that the perturbation operator (Eq. (16)) introduces anisotropic forces, since the importance of this operator is also linearly dependent on the surface tension. Perhaps a perturbation operator that would distribute the tension forces in a more isotropic way would greatly reduce the spurious currents. In other words, perhaps the whole perturbation operator is not highly isotropic, despite the fact that the discretization of the color gradient is highly isotropic. This is reminiscent of the idea of Dupin et al. [10], who adjusted the surface tension differently, depending on

**Table 7**  
Input parameters and the error obtained with the Laplace surface tension for a very high-density ratio steady bubble ( $\gamma = 10,000$ ).

Color gradient	$\gamma$	$\rho_r$	$R$	$\beta$	$\sigma_{iso}$	$E_{III}$ (%)
$\vec{F}_{III}$	10,000	1	30	0.99	$10^{-5}$	0.507

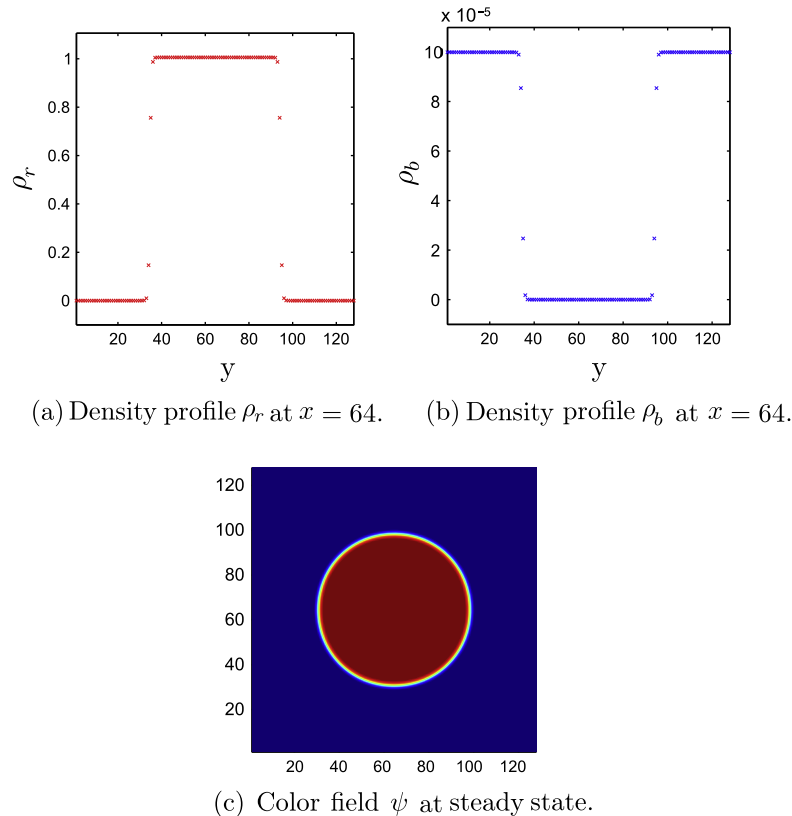


**Fig. 13.** Steady state results for the very high-density ratio steady bubble simulation ( $\gamma = 10,000$ ).

the direction of the lattice, in order to reduce the spurious currents. These currents are probably linked to the anisotropy problem at different steps of the numerical scheme. However, it is encouraging to see that, as the gradient approximation becomes more isotropic, the spurious currents are reduced. This is in agreement with the work of Ref. [37].

The results of  $\gamma = 100$  in Fig. 10 reveal that the spurious currents are stronger than with  $\gamma = 1$ . We conclude from this that an important factor influencing these currents is the density ratio. Their intensity is also roughly a linear function of the surface tension. We note that, on average and when the surface tension is low, the second order isotropic gradient does not seem capable of reducing the spurious currents. It is important to remember that the error associated with the Laplace surface tension was also high in this regime, and so was the deformation of the bubbles. This may affect the spurious currents. The fourth and sixth order isotropic gradients have almost the same behavior and produce smaller spurious currents than the second order gradients, which make them more accurate with respect to spurious currents than the other gradients.

For  $\gamma = 1000$ , the figures are very similar to the case with  $\gamma = 100$ . By increasing the density ratio, the spurious currents increase, but, this time, the sixth order isotropic gradient reduces them significantly compared to the fourth order isotropic gradient. As for the figures that show the errors with the Laplace surface tension, the spurious currents indicate that the isotropy of the color gradient is an important factor influencing accuracy.

The simulation results in Table 5 show that the effect of the interface thickness does influence the spurious currents in a significant way. Those for  $\gamma = 1000$  and  $\beta = 0.7$  are shown in Fig. 12. The spurious currents can be reduced by as much as two orders of magnitude by choosing  $\beta = 0.7$  instead of  $\beta = 0.99$ , and even more when the interface thickness is further decreased. Two alternatives are proposed for reducing the spurious currents: increase the isotropy of the color gradient discretization, or increase the interface thickness to reduce the gradient discretization errors.

### 3.4. Steady bubble: very high-density ratio

To test the stability limit and accuracy of the model, a final simulation with a very high-density ratio between the fluids was performed ( $\gamma = 10,000$ ) using the fourth order isotropic color gradient. For this simulation, the input parameters and the results are summarized in Table 7. The accuracy of the result is very good with a 0.507% error at steady state between the Laplace surface tension (Eq. (43)) and the surface tension set using the model parameters (Eq. (37)). To fully appreciate the numerical steady state solution, there is a plot of the density profile at  $x = 64$  for each fluid in Fig. 13a and b. These density profiles show that the interface is fairly clean and sharp, with a thickness of about 5–6 lattice units. The results obtained are excellent for such an extreme case. Moreover, the bubble shape at steady state is circular, as illustrated in Fig. 13c. With this model and for the steady bubble case, we can conclude that the fourth order isotropic color gradient can lead to accurate simulation of a very high-density ratio.

## 4. Conclusion

In this study, we showed that the isotropy of the color gradient is crucial to RK-type lattice Boltzmann schemes for the solution of two-phase flow problems. The simulations revealed that, when the isotropy of the color gradient is poor, the surface tension result is not reliable. For a steady bubble problem, we showed that isotropic color gradients up to second order in space are not sufficient to treat low surface tension (bubble deformation), with an average density variation of  $O(10)$ . However, the isotropic color gradients of the fourth and sixth order make it possible to accurately

simulate density ratios as high as  $O(1000)$ , depending on the surface tension. To be able to accurately simulate very low surface tension with a  $O(1000)$  density ratio, the interface thickness must also be carefully selected, and our investigation here indicates that it is possible to simulate two-phase air-to-water density ratio with the LB color gradient method. In such a case, an isotropic gradient of higher order (fourth or sixth) capable of handling a high-density ratio is worth its cost. For this model, our study also suggests that the spurious currents are mainly caused by anisotropic forces introduced at the various stages of the numerical scheme. Overall, the isotropic color gradient reduces the spurious currents, widens the range of applicability of the surface tension, and allows the accurate simulation of high-density ratios for Laplace's law. In practice, this also can be appreciated by keeping the circular shape of a two-dimensional bubble at steady state. Finally, we believe that the advantages of isotropic color gradients can be extended to all RK-type schemes.

## Acknowledgement

The authors thank the anonymous reviewers for their insightful and constructive comments. This work was supported by a grant from FQRNT "Le Fonds Québécois de la Recherche sur la Nature et les Technologies".

## References

- [1] McNamara G, Zanetti G. Phys Rev Lett 1988;61:2332.
- [2] Frisch U, Hasslacher B, Pomeau Y. Phys Rev Lett 1986;56:1505.
- [3] He X, Luo L-S. Phys Rev E 1997;56:6811.
- [4] Leclaire S, Reggio M, Trepanier J. Numerical evaluation of two recoloring operators for an immiscible two-phase flow lattice boltzmann model. May 2011, unpublished results.
- [5] Halliday I, Thompson SP, Care CM. Phys Rev E 1998;57:514.
- [6] Ginzbourg I, Adler PM. Trans Porous Media 1995;20:37–76.
- [7] Latva-Kokko M, Rothman DH. Phys Rev E 2005;71:056702.
- [8] Gunstensen AK, Rothman DH. EPL (Europhys Lett) 1992;18:157–61.
- [9] Grunau D, Chen S, Eggert K. Phys Fluids A: Fluid Dynam 1993;5:2557–62.
- [10] Dupin MM, Halliday I, Care CM. J Phys A: Math Gen 2003;36:8517–34.
- [11] Tölke J. Philos Trans R Soc Lond Ser A: Math Phys Eng Sci 2002;360:535–45.
- [12] Tölke J, Freudiger S, Krafczyk M. Comput Fluids 2006;35:820–30.
- [13] Wu L, Tsutahara M, Kim LS, Ha M. Int J Multiphase Flow 2008;34:852–64.
- [14] Shan X, Chen H. Phys Rev E 1993;47:1815.
- [15] Swift M, Orlandini E, Osborn WR, Yeomans JM. Phys Rev E 1996;54:5041.
- [16] Hao L, Cheng P. J Power Sources 2009;190:435–46.
- [17] He X, Shan X, Doolen GD. Phys Rev E 1998;57:R13.
- [18] He X, Chen S, Zhang R. J Comput Phys 1999;152:642–63.
- [19] Santos LOE, Facin PC, Philippi PC. Phys Rev E 2003;68:056302.
- [20] Kono K, Ishizuka T, Tsuda H, Kurosawa A. Comput Phys Commun 2000;129:110–20.
- [21] He X, Doolen GD. J Stat Phys 2002;107:309–28.
- [22] Reis T, Phillips TN. J Phys A: Math Theor 2007;40:4033–53.
- [23] Rothman DH, Keller JM. J Stat Phys 1988;52:1119–27.
- [24] Kumar A. J Comput Phys 2004;201:109–18.
- [25] Kuzmin A, Mohamad AA. Comput Math Appl 2010;59:2260–70.
- [26] Inamuro T, Ogata T, Ogino F. Future Gen Comput Syst 2004;20:959–64.
- [27] Inamuro T, Ogata T, Tajima S, Konishi N. J Comput Phys 2004;198:628–44.
- [28] Lee T, Lin C-L. J Comput Phys 2005;206:16–47.
- [29] Zheng HW, Shu C, Chew YT. J Comput Phys 2006;218:353–71.
- [30] Becker J, Junk M, Kehrwald D, Thömmes G, Yang Z. Comput Math Appl 2009;58:950–64.
- [31] Hou S, Shan X, Zou Q, Doolen GD, Soll WE. J Comput Phys 1997;138:695–713.
- [32] Kehrwald D. Numerical analysis of immiscible lattice BGK. Ph.D. thesis, Vom Fachbereich Mathematik der Universität; 2002.
- [33] Tiribocchi A, Stella N, Gonnella G, Lamura A. Phys Rev E 2009;80:026701.
- [34] Pooley CM, Furtado K. Phys Rev E 2008;77:046702.
- [35] Chiappini D, Bella G, Succi S, Toschi F. US Commun Comput Phys 2010;7:423–44.
- [36] Shan X. Phys Rev E 2006;73:047701.
- [37] Sbragaglia M, Benzi R, Biferale L, Succi S, Sugiyama K, Toschi F. Phys Rev E 2007;75:026702.
- [38] Chen C, Zhang D. Phys Fluids 2009;21:103301–11.
- [39] Gunstensen AK, Rothman DH, Zaleski S, Zanetti G. Phys Rev A 1991;43:4320.
- [40] LStt J. Hydrodynamic limit of lattice Boltzmann equations. Ph.D. thesis, University of Geneva; 2007.
- [41] Nourgaliev RR, Dinh TN, Theofanous TG, Joseph D. Int J Multiphase Flow 2003;29:117–69.